

---

## CONTRIBUTED PAPERS

---

# SOME APPLICATIONS OF ROTATING ANODE X-RAY GENERATORS IN THE FIELDS OF WIDE ANGLE SCATTERING, COMPTON SPECTROSCOPY AND EXTENDED X-RAY ABSORPTION FINE STRUCTURE

S. STEEB and P. LAMPARTER

Max-Planck-Institut für Metallforschung, Institut für Werkstoffwissenschaften, Seestraße 92, 7000 Stuttgart 1, Federal Republic of Germany

## 1. Introduction

In this laboratory three rotating anode X-ray generators are in permanent run:

- i) 6 kW (Type RU-3L) since 1967
- ii) 12 kW (Type RU-200 PL) since 1973
- iii) 12 kW (Type RU-200) since 1976

The scientific program mainly is concerned with the non-crystalline state of matter, namely molten and amorphous alloys. The X-ray diffraction work is done in the wide angle- and small angle-region. X-rays furthermore are used for studying the absorption behaviour (EXAFS=Extended X-ray Absorption Fine Structure) and for studying the inelastic X-ray scattering via Compton-spectroscopy. To obtain further insight into the noncrystalline structure accompanying neutron diffraction experiments in the wide and small  $Q(=4\pi/\lambda)\sin\theta$ -region are performed which led to the evaluation of partial structure factors using the method of isotopic substitution. From the numerous results only the historic experiment on amorphous  $Ni_{81}B_{19}$  [1] should be mentioned. Information about the questions of chemical bond, charge transfer and density of states is obtained by doing X-ray emission and absorption spectroscopy using an electron microprobe (Type JXA 733, Jeol) as well as synchrotron radiation (Berlin Synchrotron BESSY and German Synchrotron DESY).

Among all these activities in the following we will focus on methods which make use of rotating anode generators, namely small angle scattering, wide angle scattering, Compton spectroscopy and EXAFS.

## 2. Wide Angle Scattering

### 2.1. Solid Substances

Figure 1 shows an experimental arrangement for performing in situ wide angle experiments. Of course there are numerous applications from which we select only one, namely the determination of the short range order parameter with Mg-Cd solid solutions [2,3]. The Cowley [4] short range order parameter  $\alpha$  is a figure which for statistical distribution of the two kinds of atoms within a binary alloy is equal to zero, which is positive for segregation and which is negative for compound formation. It can be determined from the diffuse Laue scattering underlying the wide angle intensity curve obtained from binary molten or amorphous alloys or from the coordination numbers according to eqn. (1)

$$\alpha_1 = \frac{Z_{AA} - C_A Z}{C_B Z} \quad (1)$$

where  $\alpha_1$  = Cowley short range order parameter for the nearest neighbours, i.e. the first coordination sphere

$Z_{AA}$  = number of nearest neighbours of component A around an A atom

$Z$  = mean coordination number throughout the specimen

$C_A, C_B$  = atomic fraction of components A, B

$(C_A + C_B = 1)$

The short range order parameter  $\alpha$  according to Cowley is an important figure for the characterization not only of solid crystalline, but also of solid amorphous and molten specimens. For the two latter

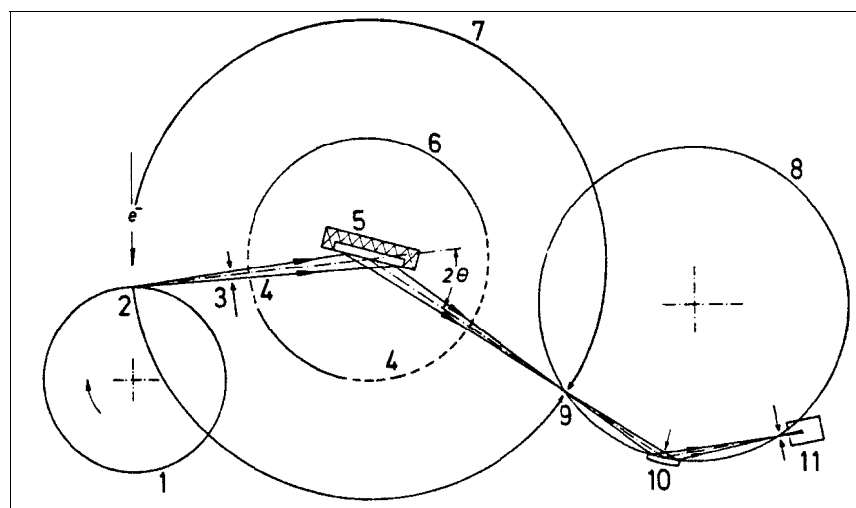


**Fig. 1.** Set up for wide angle scattering in reflection. 1, Rotating anode; 2, Focus; 3, Aperture slit; 4, Windows; 5, Furnace with specimen; 6, Vacuum chamber; 7, Goniometer circle; 8, Focussing circle; 9, Detector slit; 10, Monochromator; 11, Scintillation-counter.

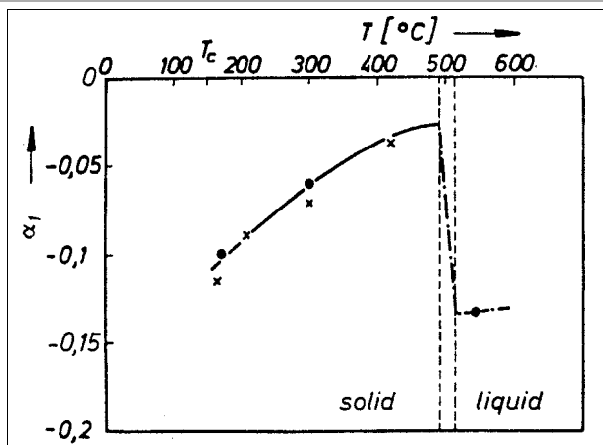


**Fig. 2.** Mg-Cd system. Temperature dependency of the short range parameter  $\alpha_1$ . (●) according to [2], (x) according to [6]

cases, especially if the atomic diameters of the atoms of the two components are different, a more meaningful figure is given by the short range order parameters according to Cargill and Spaepen [5].

With Mg-Cd alloys the temperature dependency of the short range order parameter  $\alpha_1$  was obtained as shown in Fig. 2, which means that in the solid state the tendency to compound formation becomes smaller with rising temperature. Above the temperature region (∴) in which the melting process occurs, however, the tendency for compound formation has become larger.

## 2.2 Melts

Figure 3 shows an arrangement for the wide angle-investigation of melts in transmission [7]. The

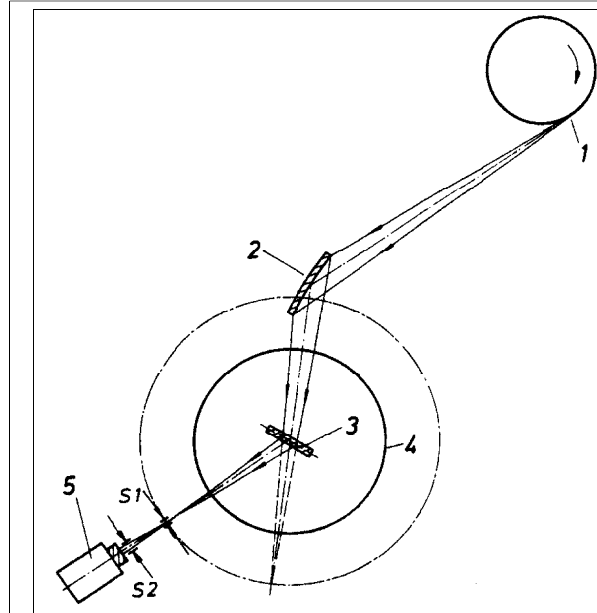


**Fig. 3.** Set up for wide angle scattering in transmission. 1, Rotating anode; 2, Monochromator; 3, Specimen within furnace; 4, Vacuum chamber; 5, Counter; S1, S2, slits.

melt is kept within beryllium windows in a sandwich construction which itself can be placed into the furnace. An alternative experimental set up for the investigation of melts is a  $\theta$ - $\theta$  diffractometer with horizontal arrangement of the melt surface and with the X-ray tube and the counter moving up and down around this surface in such a way that the angle between surface and the direction to the focus is  $\theta$ , as well as the angle between surface and the direction to

the counter. Up to now,  $\theta$ - $\theta$  arrangements only were realized with sealed-off X-ray tubes. However, the  $\theta$ - $\theta$  goniometer can only be applied with precaution for the investigation of corrosive melts [8] and melts with high vapour pressure. In these cases a closed crucible with Be windows and rotating anode generator as shown in Fig. 3 is to be preferred. The most recent investigation which we did with this arrangement was the thorough investigation of molten lithium [7].

### 2.2.1 Molten lithium

Since X-rays are scattered by electrons, the determination of the atomic arrangement within a melt by an X-ray diffraction experiment necessitates the knowledge of the spatial distribution of the electrons around the nucleus (“form factor”). For the heavier atoms this distribution is so strongly determined by the inner electrons that the electron distribution within the melt can be described with sufficient accuracy by that of the free atom. With light elements, however, such as lithium the outer electrons also play an important role for the spatial distribution of all the electrons. Thus, during the evaluation of an X-ray diffraction experiment performed with molten lithium using the electron distribution of a free atom, certain differences in comparison with the results of a corresponding neutron diffraction experiment should be expected. To verify this, a neutron and an X-ray diffraction experiment were performed with molten lithium. The atomic structure of a monoatomic melt is described by the number density function  $\rho(R)$  which represents the mean number of atoms per unit volume at the distance  $R$  from a reference atom. For large  $R$ ,  $\rho(R)$  approaches  $\rho_0$ , which is the mean number density of the melt. The corresponding variable in reciprocal space is the structure factor  $S(Q)$ . The scattering cross-section  $d\sigma/d\Omega|_{coh}^N$  for neutrons which are scattered coherently by a molten element is directly proportional to  $S(Q)$ :

$$\frac{d\sigma}{d\Omega}|_{coh}^N = N \frac{\sigma_{coh}}{4\pi} S(Q) \quad (2)$$

with

$\sigma_{coh}$  = coherent scattering cross section of a single atom

$N$  = number of atoms irradiated

$Q = (4\pi/\lambda) \sin \theta$

$\lambda$  = Wavelength

$2\theta$  = scattering angle

In contrast to the neutrons the X-rays are scattered from the electron core of the atoms. Therefore the scattering law also contains information concerning the electron distribution. The coherently scattered intensity of X-rays  $d\sigma/d\Omega|_{coh}^N$  obtained with a system of identical atoms can be obtained in electron units according to

$$\frac{d\sigma}{d\Omega}|_{coh}^X = Nf^2(Q)S(Q) \quad (3)$$

The form factor  $f(Q)$  is the Fourier transform of the electron distribution around the atomic nucleus. To obtain (eqn. 3) the so called rigid bond approach has to be used, i.e. one assumes that all electrons can be attributed to the nucleus in a definite way and are rigidly bonded. For practical use one proceeds one step further and applies for the evaluation of (eqn. 3) the form factor of the free atom as calculated by the Hartree-Fock method [9].

Thus the assumption is made that the electron distribution around the nucleus within the melt is the same as that within the gas, For metallic melts these assumptions are only valid for the inner electrons. The conduction or valency electrons are delocalized and therefore must be treated separately. Egelstaff *et al.* [10] have derived for this case the equation (4)

$$\frac{d\sigma}{d\Omega}|_{coh}^X = N[f_i^2(Q)S_{ii}(Q) + 2nf_i(Q)S_{iv}(Q) + n^2S_{vv}(Q)]$$

Equation (4) has the same structure as the scattering law of a binary alloy with the partial structure factors  $S_{ii}$ ,  $S_{iv}$ , and  $S_{vv}$ . The components in the present case are the ions  $i$  and the free or valency electrons  $v$  of the molten element.  $f_i(Q)$  means the form factor of the inner electrons,  $n$  the number of free electrons per atom.  $S_{ii}(Q) \equiv S(Q)$  describes the correlations between the ions,  $S_{vv}$  the correlations between the valency electrons, and  $S_{iv}$  the cross correlation between ions and free electrons.

These considerations show that presence of a significant electron correlation in the melt would affect the form factor compared to that one of the free atoms. Accordingly the structure factor  $S(Q)$  calculated with eqn. (3), where the form factors for the free atom is applied, would be different from the corresponding  $S(Q)$  evaluated by neutron diffraction. In the following we describe an experimental study on this question where the results of X-ray and neutron

diffraction are compared to each other. As a specimen the molten element lithium was chosen, since only for beryllium the ratio between the number of the outer and of the inner elements is larger. Lithium, however, can be handled in the molten state much easier than beryllium. To compare in a quantitative way the neutron diffraction experiment with molten lithium and the corresponding X-ray experiment. measured data also of the inelastic scattered X-rays (Compton effect) were needed, Since these data were not available in the literature they had to be measured. This was of large importance, since for light elements the intensity of the inelastically scattered X-rays is

comparable to that of the-elastically scattered radiation.

The Compton scattering was evaluated experimentally with solid lithium as described in section 3 with the result given in Fig. 4. This figure shows the intensity of the inelastically scattered X-rays in electron units with lithium using a measuring time of four hours per point. The full line shows the values calculated for the lithium atoms according to [9]. Distinct deviations are observed for  $Q < 2k_f = 2.3 \text{ \AA}^{-1}$ . This result is consistent with the measurements performed with beryllium in [11]. The dashed line in Fig. 4 shows the curve which was finally used for the correction of the X-ray diffraction experiment. The dotted line in Fig. 5 shows the structure factor of molten lithium calculated from the X-ray diffraction data using the form factor of the free atom and the experimental values for inelastic scattering from Fig. 4. For comparison the structure factor from the neutron diffraction experiment [7] is also plotted. At  $Q > 2 \text{ \AA}^{-1}$  the deviations between the two curves are smaller than 5 %. For  $Q < 1 \text{ \AA}^{-1}$ , where the height of the structure factor is very small and where the inelastic part only could be assumed, the differences are smaller than 10%. Within these two regions the differences are not significantly larger than the experimental error. Within the region  $1 < Q < 2 \text{ \AA}^{-1}$  discrepancies exist which are not fully understood. As could be shown during a critical discussion of these discrepancies in [7], there are no experimental hints on electron correlations independent of the nuclei as was assumed, for example, by Dobson [12].

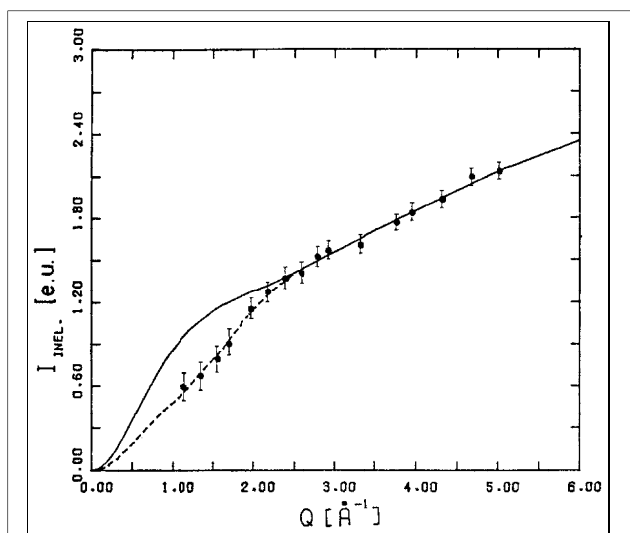


**Fig. 4.** Lithium: Integral inelastic scattering: (--- or •) Experimental result; (—) Intensity calculated for the free atom.

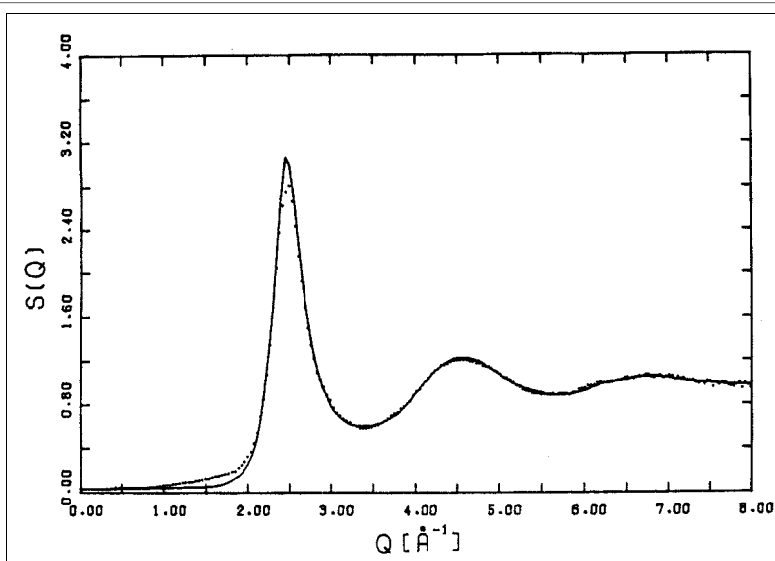


**Fig. 5.** Lithium, molten: Structure factors: (•••) X-ray diffraction (---) Neutron diffraction.

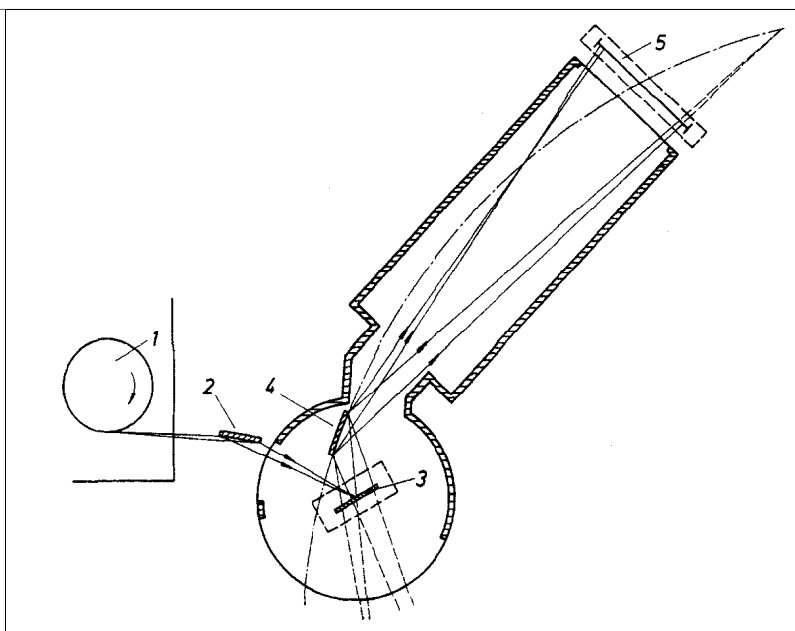


Fig. 6. Arrangement for Compton spectroscopy. 1. Rotating anode X-ray generator; 2, monochromator; 3, Specimen; 4, Analyzer; 5, Position sensitive detector.

As a conclusion of the section on wide angle scattering it should be mentioned that we just are installing an experimental set up at the RU 200 which will enable us to perform energy dispersive X-ray diffraction using a Si(Li) detector in a fixed position.

Finally it should be mentioned that in the field of molten and amorphous alloys many structures could be determined mainly by applying the method of neutron diffraction combined with isotopic substitution. For a compilation see [13].

### 3. Experimental Determination of the Inelastically Scattered X-ray Intensity

The simplest case of an inelastic X-ray scattering process is the elastic impact of an X-ray quantum to a free electron at rest. The X-ray quantum thereby loses energy and its wavelength is varied. The variation  $\Delta\lambda_0$  of the wavelength amounts to

$$\Delta\lambda_0 = 2\lambda_c \sin^2 \theta = (\lambda_c / 8\pi^2) \lambda^2 Q^2 \quad (4)$$

with

$$\lambda = h/mc = \text{Compton wavelength}$$

Since the electrons in reality are not at rest but have a certain velocity distribution, according to this simple concept a broad line around the mean wavelength shift  $\Delta\lambda_0$  is expected in the inelastic X-ray spectrum. According to eqn. (4) at small scattering

angles  $\Delta\lambda_0$  varies proportional to  $\theta$ . With finite resolution of the spectrometer the inelastic line can therefore not be separated from the elastic line at small scattering angles.

The main problem with the measurement of the inelastic scattering of X-rays is due to the very small intensity. In the past, most of the measurements were therefore performed without a primary beam monochromator. In these experiments only the scattered radiation was analyzed within a crystal spectrometer working in step scan mode. Scattered radiation arising from the Bremsstrahlung thereby forms a background which disturbs the measurement (compare [14]). Using a position sensitive detector a novel spectrometer was constructed and installed

Table 1. Data of the Spectrometer

Monochromator	Quartz 110 $\bar{1}$ 1st order
Primary wavelength	Cu-K $\alpha_1$ , $\lambda=1.54\text{\AA}$
Suppression of $\alpha_2$	$I(\alpha_2)/I(\alpha_1) < 0.1$
Analyzing crystal	Quartz 110 $\bar{1}$ 2nd order
Simultaneously detectable wavelength region	$1.5 < \lambda < 1.7\text{\AA}$
Energy resolution	$E/\Delta E = 10^3$
Scattering angle	$0^\circ < 2\theta < 150^\circ$

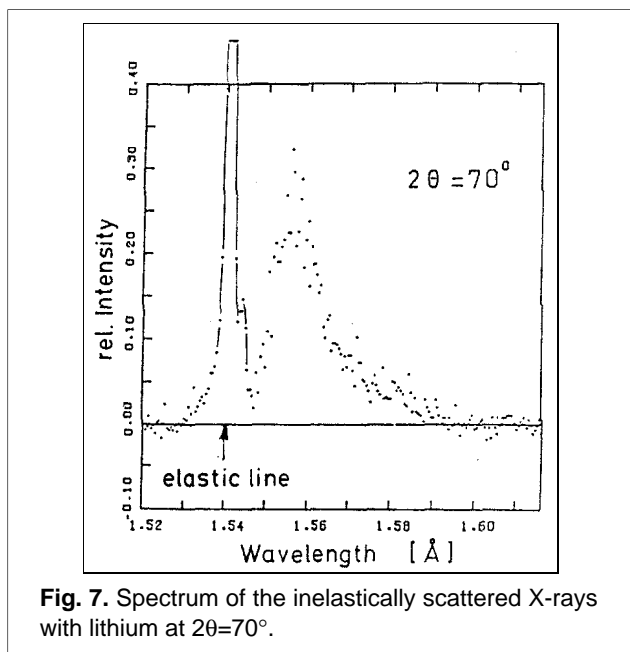


**Fig. 7.** Spectrum of the inelastically scattered X-rays with lithium at  $2\theta=70^\circ$ .

[17]. This instrument makes it possible to record the total energy spectrum at once. Thus, the measuring time can be reduced drastically and a primary beam monochromator can be applied.

Figure 6 shows the principle of the spectrometer. The beam produced within the rotating anode X-ray generator (1) is monochromatized by the monochromator (2) and is analyzed according to the energy by a curved analyzing crystal (4) after being scattered at the specimen (3). Using this method, radiation of different energy enters the position sensitive detector (5) at different positions. To avoid air-absorption and air-scattering the total beam geometry is kept in vacuum or in helium. The spectrometer is mounted on a turnable plate with the specimen mounted in the centre. The scattering angle can be varied in the region  $0^\circ \leq 2\theta \leq 150^\circ$ . Table I contains the characteristic data of the spectrometer. A similar instrument, however using photographic film instead of a position sensitive detector (PSD) was used by du Mond [15]. A spectrometer using a PSD as described above was used by Loupias et al. [16] and by Pattison et al. [17].

In contrast to the X-ray elastic diffraction experiment using Mo-K $\alpha$  radiation the determination of the inelastic X-ray scattering was performed using Cu-K $\alpha$  radiation, since the energy resolution of a crystal with a given mosaic spread increases with increasing wavelength. The presumption for this procedure is the fact that the scattering intensity only depends on the momentum transfer  $Q=(4\pi/\lambda)\sin\theta$  and not on the quantum energy of the primary beam. This

presumption is fulfilled for lithium caused by the small binding energy of the electrons. The corrections for absorption and polarization were performed in analogy with the procedure for the X-ray diffraction experiment described in section 2.2.3.

Figure 7 shows a typical result. The curve is corrected for background, absorption, polarization, and relativistic effects (Breit-Dirac-factor). For the normalization of the experimental values a curve calculated for the free atom was used, since for  $Q > 3\text{\AA}^{-1}$  no deviation from this curve was to be expected. Data as given by Fig. 7 finally led to the intensity of the inelastically scattered X-rays as given in Fig. 4 of section 2.2.2.

#### 4. Small Angle Scattering

X-ray small angle scattering (X-SAS) always occurs with a specimen consisting of a matrix with electron density  $\rho_M^e$  and of regions with electron density  $\rho_R^e$  if  $\rho_M^e - \rho_R^e \neq 0$ . For the intensity  $I(Q)$  in the small angle region stands (see e.g. [18]).

$$I(Q) = (\rho_M^e - \rho_R^e)^2 v_M v_R \cdot 4\pi \int_0^\infty \gamma_0(R) R^2 \frac{\sin QR}{QR} dR \quad (5)$$

with  $v_m$  = volume fraction of the matrix

$v_R$  = Volume fraction of the regions

$\gamma_0(R)$  = normalized correlation function

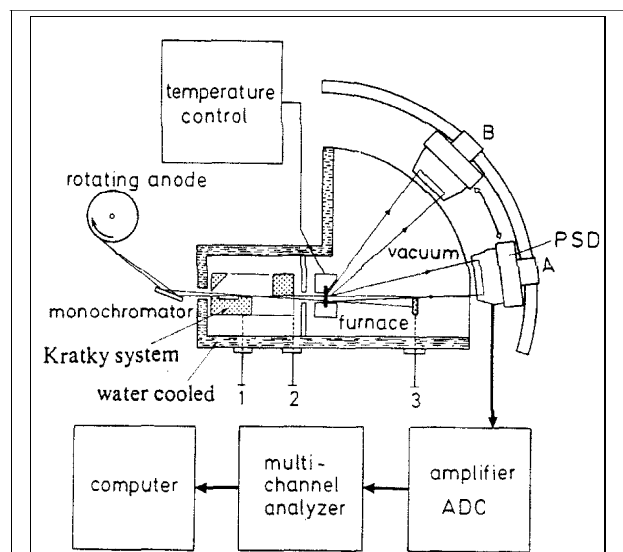


**Fig. 8.** High temperature-high vacuum-small angle X-ray scattering camera [9], outer wall water cooled, inner wall Kratky system; 1, 2, 3: micrometer screws; PSD = position sensitive detector; ADC = analog digital converter.

The electron density of an alloy can be calculated from the atomic number density  $\rho$ , and the mean number of electrons  $\bar{Z}$  per atom. Thus we obtain

$$(\rho_M^e - \rho_R^e) = \rho_M \bar{Z}_M - \rho_R \bar{Z}_R \quad (6)$$

Two extreme situations are imaginable:

i) The specimen shows density fluctuations only; eqn. (6) then becomes

$$(\rho_M^e - \rho_R^e) = \bar{Z}(\rho_M - \rho_R) \quad (7)$$

ii) The specimen shows concentration fluctuations only; eqn. (6) then becomes

$$(\rho_M^e - \rho_R^e) = \rho(\bar{Z}_M - \bar{Z}_R) \quad (8)$$

For a quantitative evaluation of eqn. (5) the intensity is needed in absolute units, i.e., it has to be normalized. A very convenient method for the case of amorphous or molten substances is given by a measurement also in the large  $Q$ -region with the same instrument to perform the normalization procedure. This is because only in that  $Q$ -region the run of the corresponding intensity curves is monotonically and thus can be adjusted to the run of  $\langle f^2 \rangle = C_A f_A^2 + C_B f_B^2$ . The demand to be able to measure at large  $Q$ 's led to the construction of a small angle camera as shown in Fig. 8 which enables. To perform measurements not only in the small angle region but also in the wide angle region.

A very powerful combination is a rotating anode X-ray generator (Type RU-200, Rigaku Denki, Tokyo) and a position sensitive detector PSD (Braun, Garching) especially if one works with monochromatized radiation (graphite monochromator type Stoe, Darmstadt). This causes a considerable reduction of primary intensity and thus the ability of the position sensitive detector to measure the whole small angle region simultaneously is advantageous. Within the water cooled camera we recognize the Kratky system which in itself is watercooled, too. It can be adjusted from outside the vacuum chamber by two micrometer screws 1 and 2. Between Kratky system and furnace a heat shield is placed. The specimen contained in a flat crucible can be pulled out of the hot furnace for a calibration measurement of the apparatus without specimen. The primary beam stop is adjustable by micrometer screw 3. The position B of the PSD serves to measure the intensity at large  $Q$ .

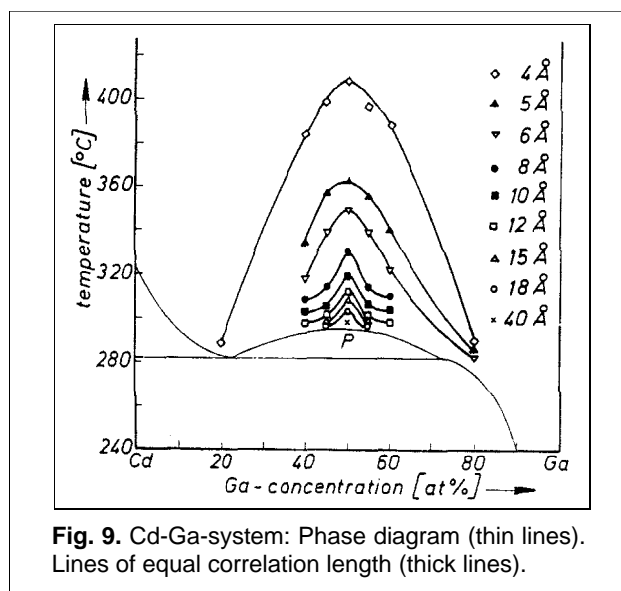


Fig. 9. Cd-Ga-system: Phase diagram (thin lines). Lines of equal correlation length (thick lines).

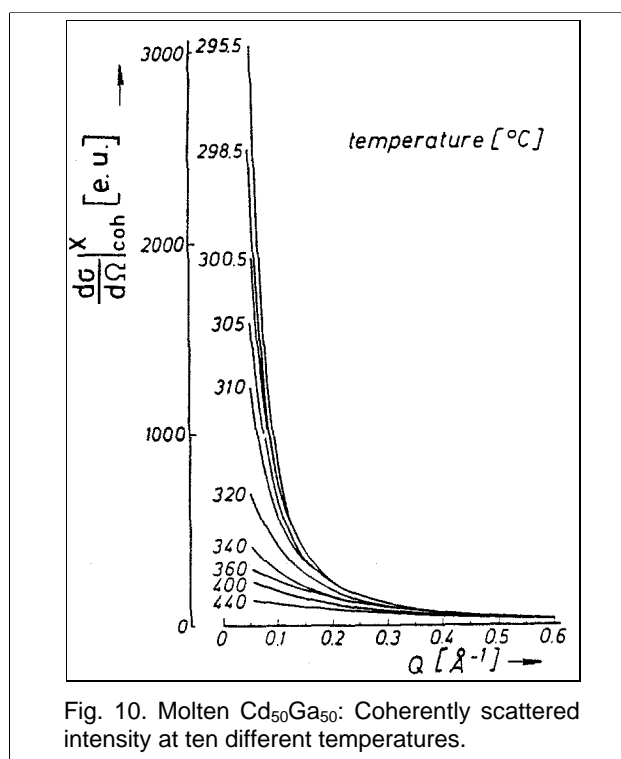


Fig. 10. Molten  $Cd_{50}Ga_{50}$ : Coherently scattered intensity at ten different temperatures.

With the apparatus as shown in Fig. 8 (see Ref. [19], for example) for the first time X-ray small angle scattering could be observed with molten alloys, namely Al-Sn alloys [20]. A Guinier plot of the intensity [21], i.e., plotting  $\ln I$  versus  $Q^2$  yielded a straight line the gradient of which tells us that the corresponding melt contains regions with diameters of about 10 Å.

In Fig. 9 the results of an investigation with Cd-Ga melts are presented [22]. The figure shows the

phase diagram (thin lines) containing a two phase field in which two melts coexist and which culminates at the so called critical point P. In the single melt region above P our results are presented by temperature concentration curves (thick lines) each of them being representative for a certain correlation length. Thus the single melt region is not really homogeneous but contains correlated zones, the correlation length of which can be determined according to the Ornstein-Zernike-theory [23] by plotting the reciprocal intensity  $I_{coh}^{-1}$  vs.  $Q^2$  and thus obtaining the correlation length. This evaluation is based on the coherently scattered intensities  $I_{coh}(Q)$  in electron units which are plotted vs.  $Q$  in Fig. 10 for the  $Cd_{50}Ga_{50}$ -melt at ten different temperatures. The investigation of the crystallization process of amorphous binaries during in situ heat treatment is another modern application of the fast X-ray small angle scattering method which is only possible by using rotating anodes and PSD's. We mention the recent investigation on the crystallization of amorphous  $Mg_{76}Zn_{24}$  [19].

For a complete analysis of the medium range structure of amorphous binaries the X-SAS method has to be supplemented by the neutron SAS method together with the isotopic substitution method. Thus it became possible for the first time with amorphous  $Ni_{80}P_{20}$  to split up the intensity curves into partial structure factor curves which allow to decide between the two possibilities represented by eqns. (7) and (8). These results are presented in Ref. [24].

As a conclusion of the section on small angle scattering it should be mentioned that we just are installing a small angle apparatus with a total length of ten meters using not a Kratky system but pin hole geometry as well as PSD and an rotating anode X-ray generator. Thus the rather ambiguous desmearing procedure can be avoided.

### 5. X-ray Absorption (EXAFS)

The atomic scale structure of metallic glasses has been investigated up to now most frequently by means of conventional methods such as X-ray, electron, and neutron diffraction [13, 25, 26]. In the last years, however, measurements of the fine structure of X-ray absorption edges (EXAFS) have been used to an increasing extent for the determination of local atomic arrangements [27-31].

Compared with the usual diffraction methods, EXAFS has the advantage of giving information

concerning the local atomic arrangement around a specific atomic species. In contrast to this, a diffraction experiment yields information of atomic arrangements around a reference atom which represents an average of all atomic species present in the specimen.

For energies larger than a characteristic threshold energy, each element shows a sudden rise of the X-ray absorption coefficient forming an edge. The appearance of this edge is related with the fact that for energies larger than this threshold energy the excitation of electrons out of an inner shell becomes possible. Phenomena related with this edge therefore allow to make statements concerning the specific atomic species.

In an EXAFS experiment, the quantity of interest is the modulation  $\chi(k)$  with  $k=2\pi/\lambda$  of the X-ray absorption coefficient in the energy range just above an absorption edge. This modulation extends over an energy range of several hundred electron volts above the absorption edge.

According to present ideas, the appearance of this modulation is due to local interference effects. of the photoelectrons produced during the absorption process. Such a photoelectron travels as a wave away from the atom ionized during the absorption process and it can be backscattered to the original atom by neighbouring atoms. The modulations observed in the X-ray absorption coefficient can be explained as an

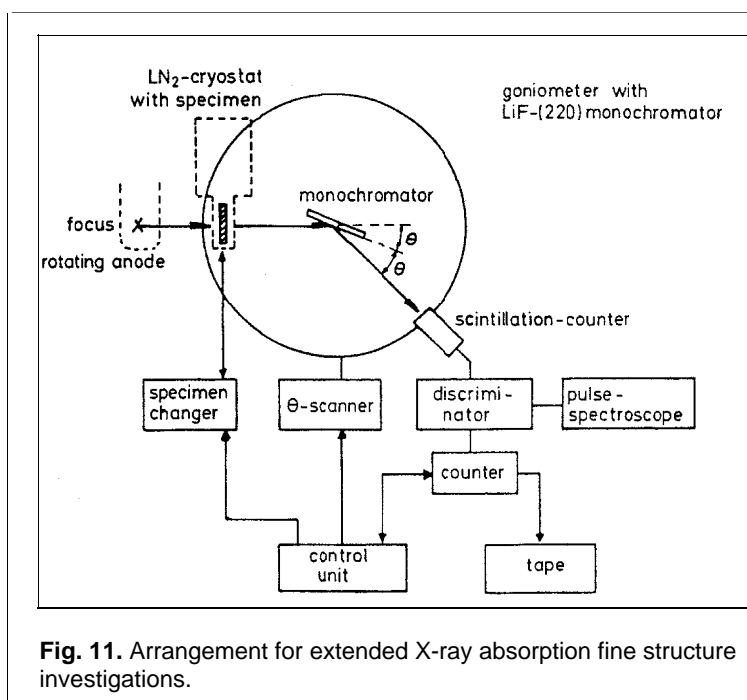


**Fig. 11.** Arrangement for extended X-ray absorption fine structure investigations.

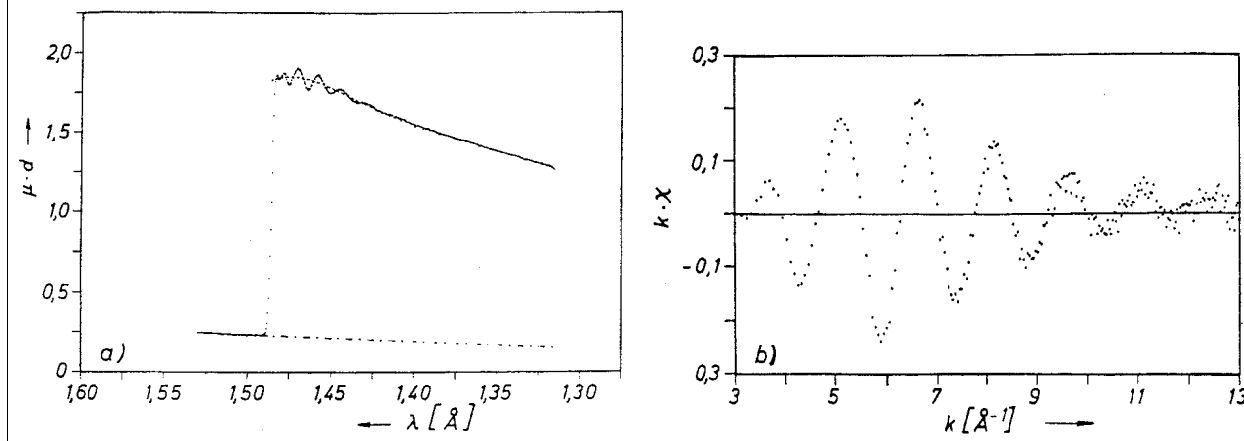


**Fig. 12.** Amorphous  $\text{Ni}_{81.5}\text{B}_{18.5}$  ( $T=80\text{K}$ ): Normalization of absorption spectra.  
 a) Ni-K absorption spectrum  
 b) EXAFS modulation from a).

interference between the outgoing and the backscattered wave [32-35].

In reverse, following the analysis of this modulation one can draw conclusions concerning the local atomic arrangement in the environment of the atomic species under consideration [36-39].

Figure 11 shows an EXAFS apparatus which works in connection with a 6 kW-rotating anode X-ray generator with Ag-target since 1979. The absorption coefficient  $\mu(E)$  is obtained by measuring the intensity once with specimen and once without specimen for a certain energy  $E$  of the radiation which is determined by the angle  $\theta$ . In the first case one obtains  $I$  and in the second case  $I_0$ . Thus we obtain the absorption coefficient as

$$\mu(E) = \frac{1}{d} \ln \frac{I_0(E)}{I(E)} \quad (9)$$

with  $d$ = thickness of the absorber.

During the measurements the samples are mounted in a liquid nitrogen cryostat and held at a temperature of 80 K. A flat LiF-(220) crystal is used for the spectral analysis of the radiation. Dependent on its angular position, this crystal selects out of the incident white radiation a fixed wavelength  $\lambda$  according to Bragg's relation. Monochromatic radiation can be provided therefore by variation of the angle  $\theta$ . The spectral resolution  $\Delta\lambda/\lambda$  has a value of about  $1.4 \times 10^{-3}$ , which was tested by measuring the width of the  $\text{W}_{L\alpha 1}$ -line, W being tungsten. The EXAFS spectra are recorded by scanning the angle  $\theta$  in steps of  $\Delta\theta=0.01^\circ$ . At each data point the

transmitted intensity  $I$  as well as the incident intensity  $I_0$  is measured, the latter by pulling the sample out of the beam by means of a special setup installed in the cryostat. Therefore, possible long-periodic intensity fluctuations of the radiation source, can be compensated. To achieve good statistical accuracy,  $10^6$  counts are preselected for each data point. The data processing is done using a PDP 11/34 computer.

Figure 12a shows the Ni-K absorption edge of amorphous  $\text{Ni}_{81.5}\text{B}_{18.5}$  which exhibits distinct oscillations around the dashed line, i.e., the EXAFS modulations.

The extraction of the EXAFS modulation  $\chi(k)$  is done in the usual way by fitting a polynomial to the measured spectra in the energy region above the absorption edge in such a way that it describes  $\mu \cdot d$  which would be observed in the absence of EXAFS modulations. Polynomials with 4th to 6th degree have turned out to be optimal for this purpose. By this procedure the "base line" of the spectra is obtained (dashed line in Fig. 12a), which finally is represented by the zero line of the EXAFS spectrum as presented in Fig. 12b.

The EXAFS modulation is superposed as a weak signal on a very high background, Therefore, the function  $\chi(k)$  has much more noise than the total spectrum measured with a statistical accuracy of 0.2%. Thus a smoothing procedure is necessary before further interpretation of the data. The smoothing is done with a "cubic spline-fit" algorithm, which approximates the data sectionally by polynomials of 3rd degree. The function obtained in this way is the starting point for all further interpretations performed.

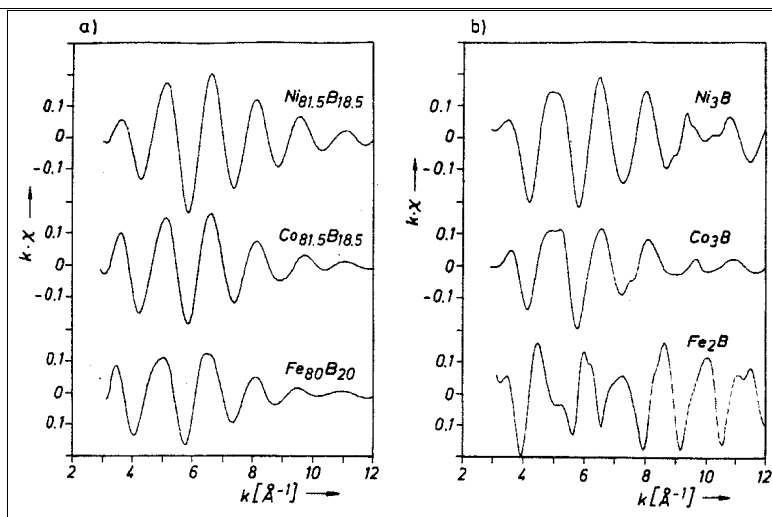


**Fig. 13.** EXAFS spectra of amorphous and crystalline transition metal boron alloys. a) amorphous alloys; b) crystalline compounds.

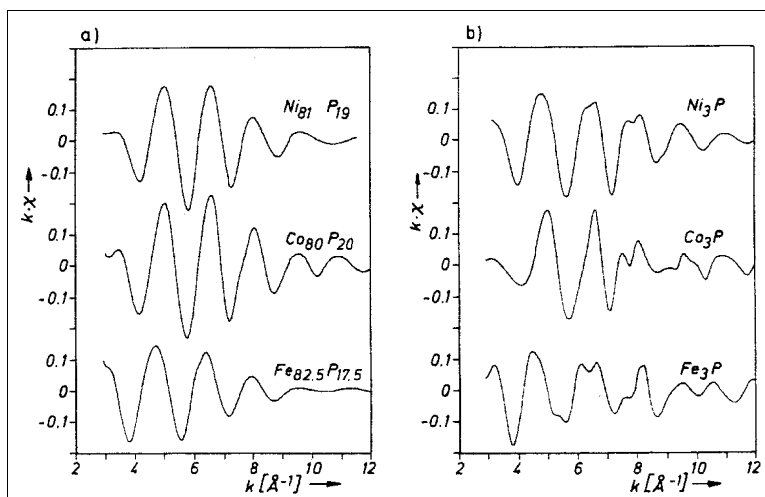


**Fig. 14.** EXAFS spectra of amorphous and crystalline transition metal phosphorous alloys. a) amorphous alloys; b) crystalline compounds.

In Figs. 13 and 14 the spectra of amorphous transition metal based B and P alloys (TM) are compared with those of the corresponding crystalline phase. The EXAFS spectra of the amorphous B and P alloys in Figs. 13a and 14a all have a very similar shape. They consist of damped oscillations with a relatively uniform frequency. The absence of higher frequency portions in these spectra is due to the absence of strong correlations between the central atom and the more distant neighbours in the amorphous state.

One can get more information comparing the EXAFS spectra measured with the amorphous alloys and those of the crystalline elements Fe, Co and Ni (not shown here) as well as those of related crystalline

B and P alloys (Figs. 13b and 14b). Here one can recognize in some cases a large similarity between the spectra of the amorphous alloys and those of the corresponding crystalline compounds. Especially the amplitude of the EXAFS modulation has a comparable magnitude in these cases, whereas for the pure elements the magnitude is greater by a factor 3-4. Altogether, the spectra of the crystalline TM alloys show a more detailed structure, which is due to larger long range order compared with the case of the amorphous alloys, because the higher-frequency components in the EXAFS spectrum are caused by the contributions of the more distant neighbouring atoms.

The best correspondence between the amorphous alloys and the crystalline compounds is found in the

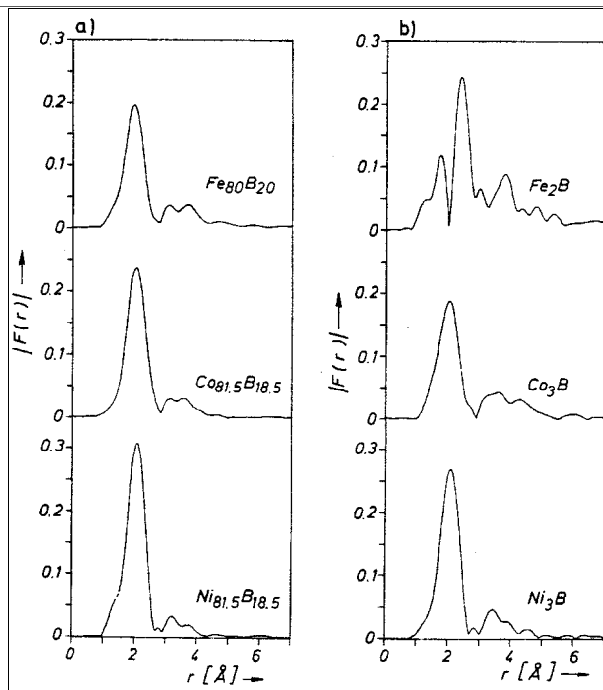


**Fig. 15.** Magnitude of the Fourier transform of the EXAFS spectra of amorphous and crystalline transition-boron alloys.  
a) amorphous alloys; b) crystalline compounds

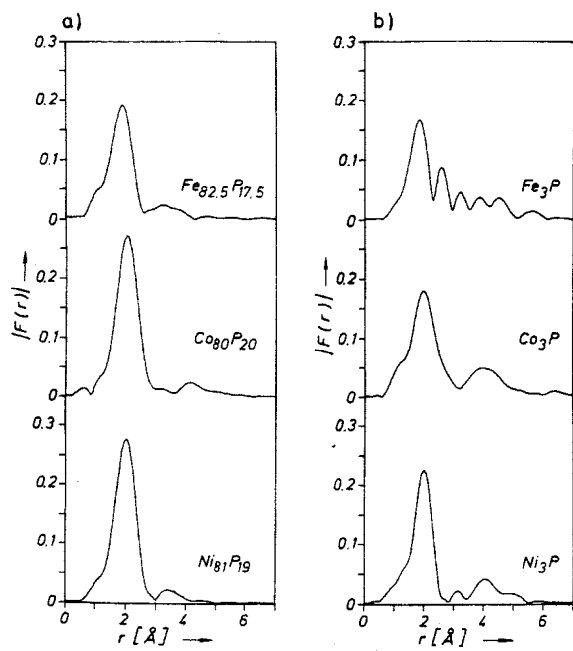


**Fig. 16.** Magnitude of the Fourier transform of the EXAFS spectra of amorphous and crystalline transition-phosphorous alloys.  
a) amorphous alloys; b) crystalline compounds

case of the Ni alloys. With the Co alloys, the correspondence is relatively good too, whereas the greatest differences occur with the Fe alloys. Especially the composition  $\text{Fe}_2\text{B}$  shows the largest deviations, which can be related to the fact that in this case the metalloid concentration also shows the largest difference and therefore, with respect to the chemical point of view there is also the smallest relation between the crystalline reference substance and the amorphous alloy. This example shows clearly, that for EXAFS investigations it is very important to use for the purpose of reference measurements only such crystalline substances which are chemically very close to the system under investigation.

The fact, that the amplitude of the EXAFS modulation in the amorphous and in the crystalline TM alloys is in both cases reduced by the same factor in comparison with the spectrum of the corresponding pure element shows that the nearest-neighbour distances in these systems show a larger spread than in the case of the pure elements whereas the mean distances  $R_1$  have approximately the same value. By comparing the EXAFS spectra it can be derived therefore, that the arrangement of nearest neighbours in the amorphous systems and in the corresponding crystal-

line  $\text{T}_3\text{M}$ -compounds shows a certain degree of similarity.

At this point the paper [41] should be mentioned, where the EXAFS spectrum of amorphous  $\text{Co}_{76}\text{P}_{24}$  (produced by electrochemical deposition) is compared with the spectra of crystalline  $\text{Fe}_3\text{P}$ ,  $\text{Fe}_2\text{P}$ , and  $\text{Co}_2\text{P}$ . The comparison with the spectra obtained during the present work shows especially in the case of the crystalline substances a more smooth run with much lower amplitudes in [41]. This probably can be ascribed to the higher sample temperatures applied in [41].

#### Fourier Transforms

As well as the EXAFS spectra of the amorphous B and P alloys also their Fourier transforms presented in Fig. 15 and Fig. 16 are quite similar among each other. In the case of the Ni and Co systems their striking relationship to the corresponding crystalline  $\text{T}_3\text{M}$  compounds is to be mentioned, too. The largest differences again occur in the case of the Fe alloys. Especially with the compound  $\text{Fe}_2\text{B}$  the first peak in  $|F(r)|$  is clearly split into two subpeaks.

As in the case of the crystalline elements Fe, Co, and Ni the peaks corresponding to the first coordination shell in Fig. 15 and Fig. 16 yield the dominating

contribution to  $|F(r)|$ . Compared with the amorphous alloys, the crystalline TM alloys clearly yield more contributions from more distant coordination shells which however are much less pronounced than in the case of the pure elements.

The metal-metal distances as well as the metal-metalloid distances give contributions to the first peak of the Fourier transforms. The difference between these distances, however, is not spatially resolved in  $|F(r)|$ . The main reason for this is expected to be the low scattering power of the metalloid atoms compared to that of the metal atoms. The shoulders occurring in some cases at the front side of the first peak in the region of  $0.8\text{\AA}$ - $1.2\text{\AA}$  must not be regarded as metal-metalloid distances, because their shape depends strongly on the polynomial degree chosen for the normalization of the spectra. Therefore they have no real physical meaning.

In the case of the amorphous transition metal-boron alloys, the second peak in  $|F(r)|$  is split into two subpeaks. This effect is most obvious for amorphous  $\text{Fe}_{80}\text{B}_{20}$ , whereas the splitting with  $\text{Co}_{81.5}\text{B}_{18.5}$  and  $\text{Ni}_{81.5}\text{B}_{18.5}$  is less pronounced in accordance to results reported in [26]. The amorphous transition metal-phosphorous alloys, however, show from X-ray and neutron diffraction more smeared out structures beyond the first coordination shell.

Such splitting of the second peak in  $|F(r)|$  has been found by other authors with EXAFS investigations on amorphous alloys of the type  $\text{Fe}_{40}\text{Ni}_{40}\text{B}_{20-\chi}\text{P}_{\chi}$  (with  $\chi=0-20$ ) [29, 30].

In the case of the crystalline TM compounds, the Fourier transforms  $F(r)$  exhibit beyond the first coordination shell larger amplitudes and longer extension in  $r$ -space than the corresponding amorphous alloys. This can be attributed to the more pronounced long range order in these systems.

Recently the K-absorption edge of the element boron was measured too [42] in pure boron as well as in F-B metallic glasses. Therefore very low energy X-rays were necessary, which of course by a rotation anode generator cannot be supplied. Thus these measurements were done at the Berlin Synchrotron (BESSY).

In connection with absorption experiments attention should be drawn on a paper which recently was published in this Journal [43].

## 6. Conclusion

Some applications of rotating anode X-ray generators are presented, all of them being characterized by the demand record within reasonable measuring times the quantitative intensity of X-rays after interaction with the investigated specimens.

These applications are:

- i) the determination of the temperature dependent short range order parameter with Mg-Cd solid solubilities,
- ii) wide angle scattering with molten lithium
- iii) Compton spectroscopy with molten lithium
- iv) small angle scattering with molten Al-Sn alloys,
- v) small angle scattering with molten Cd-Ga alloys, and
- vi) extended X-ray absorption fine structure (EXAFS) with amorphous  $\text{Fe}_{82.5}\text{P}_{17.5}$ ,  $\text{Co}_{80}\text{P}_{20}$ ,  $\text{Ni}_{81}\text{P}_{19}$ ,  $\text{Fe}_{80}\text{B}_{20}$ ,  $\text{Co}_{81.5}\text{B}_{18.5}$ ,  $\text{Ni}_{81.5}\text{B}_{18.5}$ , and crystalline  $\text{Fe}_3\text{P}$ ,  $\text{Co}_3\text{P}$ ,  $\text{Ni}_3\text{P}$ ,  $\text{Fe}_2\text{B}$ ,  $\text{Co}_3\text{B}$  as well as  $\text{Ni}_3\text{B}$ .

## 7. References

- [1] Lamparter, P., Sperl, W., Steeb, S., and Blétry, J., Z. Naturforschung **37a** (1982) 1223.
- [2] Boos, A., Steeb, S., Z. Naturforschung **32a** (1977) 1229.
- [3] Boos, A. Lamparter, P., Steeb, S., Z. Naturforschung **32a** (1977) 1222.
- [4] Cowley, J. M., J. Appl. Phys. **21** (1950) 24.
- [5] Cargill, III., G. S., Spaepen, F., J. Non Cryst. Solids **43** (1981) 19.
- [6] Frantz, C., Le Caer, G., Gantois, M., J. Appl. Cryst. **3** (1970) 123.
- [7] Olbrich, H., Ruppertsberg, H., Steeb, S., Z. Naturforschung **38a** (1983) 1328.
- [8] Sedelmeyer, B., Doctor thesis, Universität Stuttgart (1985).
- [9] Hubbel, J. H., Veigele, Wm. J., Briggs, E. A., Brown, R. T., Cromer, J. T., and Howerton, R. J., J. Phys. Chem. Ref. Data **4** (1975) 471.
- [10] Egelstaff, P. A., March, N. H., and McGill, N. C., Can. J. Phys. **52** (1974) 1651.
- [11] Schülke, W., Berg, U., and Brümmer, O., Phys. Stat. Sol. **35** (1969) 227.
- [12] Dobson, P. J., J. Phys. **C11** (1978) L295.
- [13] Steeb, S., Lamparter, P., J. Non Cryst. Solids **61** (1984) 237.
- [14] Perrin, R. C., Taylor, R., and March, N. H., J. Phys. F5 (1975) 1490.

- [15] Williams, B., "Compton Scattering", McGraw Hill, London 1977.
- [16] Loupiau, G and Petiau, J., J. Phys. **41** (1980) 265.
- [17] Pattison, P., Bleif, H.-J., and Schneider, J. R., J. Phys. **114** (1981) 95.
- [18] Glatter, O., Kratky, O., "Small Angle X-Ray Scattering", Academic Press, London (1982).
- [19] Schaal, M., Diplom thesis, University Stuttgart (1985).
- [20] Hezel, R. Steeb, S., Z. Naturforschung **25a** (1970) 1085.
- [21] Guinier, A., Fournet, G., Small Angle Scattering of X-Rays, J. Wiley & Sons, New York (1955).
- [22] Hermann, G., Rainer-Harbach, G., Steeb, S., Z. Naturforschung **35a** (1980) 938.
- [23] Ornstein, L. S., Zernike, F., Proc. Acad. Sci., Amsterdam **17**, (1914) 793.
- [24] Schild, K., Frisius, F., Lamparter, P., Steeb, S., Z. Naturforschung **40a** (1985) 551.
- [25] Nold, E., Lamparter, P., Olbrich, H., Rainer-Harbach, G., and Steeb, S., Z. Naturforschung **36a** (1981) 1032.
- [26] Lamparter, P., Nold, E., Rainer-Harbach, G., Grallath, E., and Steeb, S., Z. Naturforschung **36a** (1981) 165.
- [27] Raoux, D., et al., Revue Phys. Appl. **15** (1980) 1079.
- [28] Werner, A., Doctor thesis, Universität Kiel (1979).
- [29] Wong, J., Lytle, F. W., Greigor, R. B., Liebermann, H. H., Walter, J. L., and Luborsky, F. E., General Electric Technical Information Series Rep. No. 78CRD253, Feb. 1979.
- [30] Crescenzi, M. de, Balzarotti, A., Comin, F., Inoccia, L., Mobilio, S., and Bacci, D., Fourth International Conference on Liquid and Amorphous Metals, Grenoble **C8** (1980) 238.
- [31] Schumückle, F., Lamparter, P., and Steeb, S., Z. Naturforschung **37a** (1982) 572.
- [32] Sayers, D. E., Lytle, F. W., and Stern, E. A., Adv. X-Ray Anal. **13** (1970) 248.
- [33] Stern, E. A., Phys. Rev. **B10** (1974) 3027.
- [34] Lee, P. A., and Pendry, J. B., Phys. Rev. **B11** (1975) 2795.
- [35] Ashley, C. A., and Doniach, S., Phys. Rev. **B11** (1975) 1279.
- [36] Sayers, D. E., Stern, E. A., and Lytle, F. W., Phys. Rev. Lett. **27** (1971) 1204.
- [37] Lytle, F. W., Sayers, D. E., and Stern, E. A., Phys. Rev. **B11** (1975) 4825.
- [38] Stern, E. A., Sayers, D. E., and Lytle, F. W., Phys. Rev. **B11** (1975) 4836.
- [39] Hayes, T. M., Sen, P. N., and Hunter, S. H., J. Phys. **C9** (1979) 4375.
- [40] Schmückle, F., Doctor thesis, Universität Stuttgart (1981).
- [41] Cargill III, G. S., Conference proceedings of the 4th Int. Conference on Rapidly Quenched Metals, held at Sendai, Japan, August 1981.
- [42] Hertlein, E., Diplom thesis, Universität Stuttgart (1985).
- [43] Ravet, M. F., Krill, G., Rigaku Journal **2(2)** (1985) 3.